Concentric Necklace Nanolenses for Optical Near-Field Focusing and Enhancement

Alyssa J. Pasquale,[†] Björn M. Reinhard,[‡] and Luca Dal Negro[†,*]

[†]Department of Electrical and Computer Engineering and Photonics Center, Boston University, 8 Saint Mary's Street, Boston, Massachusetts 02215, United States and
[‡]Department of Chemistry, Boston University, 590 Commonwealth Avenue, Boston, Massachusetts 02215, United States

ABSTRACT In this paper, we design and analyze concentric necklace nanolenses (CNNLs) which consist of metal nanoparticle dimers placed in the center of one or more concentric rings of plasmonic necklaces. We use three-dimensional finite-difference time-domain simulations, electron-beam lithography fabrication, dark-field scattering analysis, and surface-enhanced Raman scattering (SERS) measurements to investigate the far-field scattering and near-field light localization properties of CNNLs. Using these methods, we show that CNNLs display far-field scattering properties that arise from coupling between the dimer and surrounding necklace(s), leading to two pronounced peaks in single-necklace CNNLs and three pronounced peaks in double-necklace CNNLs. In our near-field analysis, we find that the number of particles in the surrounding necklace is an important degree of freedom in the optimization of near-field intensity within the dimer hot-spot region. By using CNNLs where the necklace diameters have a diameter equal to an integer multiple of the resonance wavelength of the isolated dimer times a constant scaling factor, the intensity of near-fields can be optimized for all geometries over a broad-band wavelength range. Using optimized geometries, we perform SERS experiments on CNNLs coated with a pMA monolayer and demonstrate 7× Raman enhancement in the single-necklace CNNL and 18× enhancement in the double-necklace CNNL over the reference dimer antenna geometry, with an average Raman enhancement value of approximately 7×10^5.

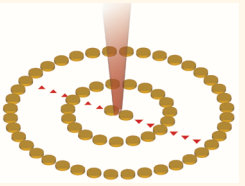

KEYWORDS: surface-enhanced Raman scattering · SERS · electron-beam lithography · plasmonics · nanoparticles · plasmonic arrays · nanolens

The engineering of the light scattering and near-field localization properties of plasmonic nanostructures plays a key role in developing more efficient sensors, optical antennas, and nanofocusing elements for molecular spectroscopy. The resonant optical responses of metallic nanoparticles can be largely tuned and enhanced for device applications by a careful design of the particle morphology,[1] by nanostructuring metallic thin films into nanohole arrays,[2] or by utilizing arrays of nanoparticles arranged in various geometries.[3−5] In particular, nanoparticle cylinders arranged in loops, referred to as "oligomers" or "necklaces", have been studied due to their ability to give rise to controllable Fano-type resonances,[6−11] magnetic plasmon response,[12,13] as well as photonic−plasmonic coupling leading to polarization insensitive near-field enhancement.[14]

Focusing and concentration of light at the nanoscale have recently emerged as topics of great interest[15−20] in plasmonics for a variety of device applications.[21−23] In particular, it has been shown that plasmonic dimers, which consist of nanoparticles separated by subwavelength gaps, give rise to highly concentrated electromagnetic fields in their nanoscale gap region, which is of paramount importance for sensing techniques such as surface-enhanced Raman scattering.[24−26] By efficiently funneling optical radiation into nanometer-sized subwavelength volumes, metallic nanoparticles greatly enhance the intensity of near-fields and surpass the spatial resolution achievable by conventional dielectric lenses, providing exciting new possibilities in nanoscale optical engineering. Optical nanoantennas have already been shown to improve the performance of solar cells and photodetectors[27−29] and can radically affect imaging and optical sensing technologies in the near future. Concentric geometries such as bulls eyes, metal films, and nanoshells have been recently studied in the broader context of plasmonic nanoantennas[30] and nanolenses[31−33] for sensing and spectroscopic applications.

In this paper, we combine nanoparticle dimers and concentric plasmonic necklaces to increase the near-field enhancement at the nanoscale dimer gap region by engineering photonic−plasmonic coupling in the necklace geometry. We make use of three-dimensional finite-difference time-domain (3D FDTD) simulations, dark-field spectroscopy, and surface-enhanced Raman scattering (SERS) to investigate the

* Address correspondence to dalnegro@bu.edu.

Received for review March 6, 2012 and accepted April 26, 2012.

Published online April 26, 2012
10.1021/nn301000u

far-field scattering and near-field properties of Au nanoparticle concentric necklace nanolenses. We demonstrate their nanolensing properties and suitability for Raman sensing applications.

RESULTS AND DISCUSSION

Concentric Necklace Nanolenses. Concentric necklace nanolenses (CNNLs) are generated by placing a dimer at the center of one or more nanoplasmonic necklaces. These necklaces are circular loops of Au nanocylinders of constant diameter (150 nm) and edge-to-edge spacing (25 nm) such that the angle between each nanocylinder is 360° divided by the number of particles in the necklace.[14] In this manner, the overall diameter of the necklace can be tuned by changing the number of constituent Au particles.

We show scanning electron micrographs (SEM) of fabricated CNNLs as well as a dimer array in Figure 1. We show in (a) isolated dimers of diameter 150 nm and gap spacing 25 nm with center-to-center separation of 2 μm to avoid radiative coupling. These dimers are then embedded into the center of a heptadecagon (17-particle) necklace in Figure 1 as an array in (b) and close-up in (c). This geometry is further embedded concentrically into a tetracontagon (40-particle) necklace in Figure 1d,e. All array scale bars correspond to 1 μm, with the scale bars in Figure 1c,e corresponding to 200 nm. All CNNLs are spaced 4 μm center-to-center to avoid coupling between adjacent CNNLs, with each array area measuring 50 μm $\times$ 50 μm. These micrographs demonstrate excellent agreement between the targeted geometric parameters over our pattern area.

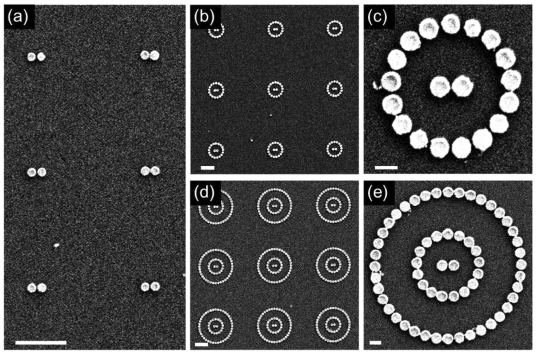

Figure 1. SEM micrographs of (a) dimer array; (b) dimer/heptadecagon array and (c) close-up; (d) dimer/heptadecagon/tetracontagon array and (e) close-up. Scale bars in (a,b,d) bars are 1 μm, and scale bars in (c,e) correspond to 200 nm.

In what follows, we will examine the far-field scattering and near-field properties of CNNLs, with particular emphasis on optimizing the structures for maximum intensity enhancement in the dimer gap region (*i.e.*, nanolensing). The optimization parameters are the number of concentric necklaces as well as the number of particles within each necklace. Experimental measurements using dark-field scattering and surface-enhanced Raman scattering will be used to validate our predictions.

Far-Field Scattering. In this section, we will focus on the far-field properties of dimer and CNNL geometries. We first turn our attention to the scattering efficiency of single- and double-necklace CNNLs with excitation polarized along the longitudinal axis of the dimer. In Figure 2a, we show the calculated scattering efficiency for an individual dimer, heptadecagon, and dimer/heptadecagon CNNL as a representative example. The heptadecagon features a strong scattering peak at 677 nm and two weaker scattering peaks at 856 and 995 nm. In general, plasmonic necklaces have been shown to support at least two scattering peaks corresponding to hybridized dipolar modes, with some necklaces exhibiting isolated strong peaks as well as weaker peaks (such as the pentagon, heptadecagon, and enneadecagon geometries).[9,14] In contrast to the necklaces, the isolated dimer supports a single scattering peak centered at 796 nm. When these two geometries are coupled into the CNNL, two predominant scattering peaks arise. The high-energy peak corresponds to the main scattering peak of the heptadecagon

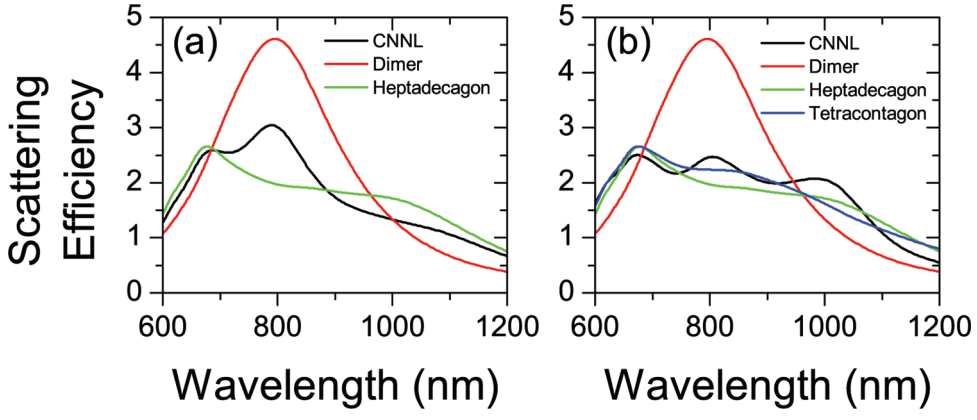

Figure 2. (a) Calculated scattering efficiency spectra of an isolated dimer, heptadecagon, and dimer/heptadecagon CNNL. (b) Calculated scattering efficiency spectra of an isolated dimer, heptadecagon, tetracontagon, and dimer/heptadecagon/tetracontagon CNNL.

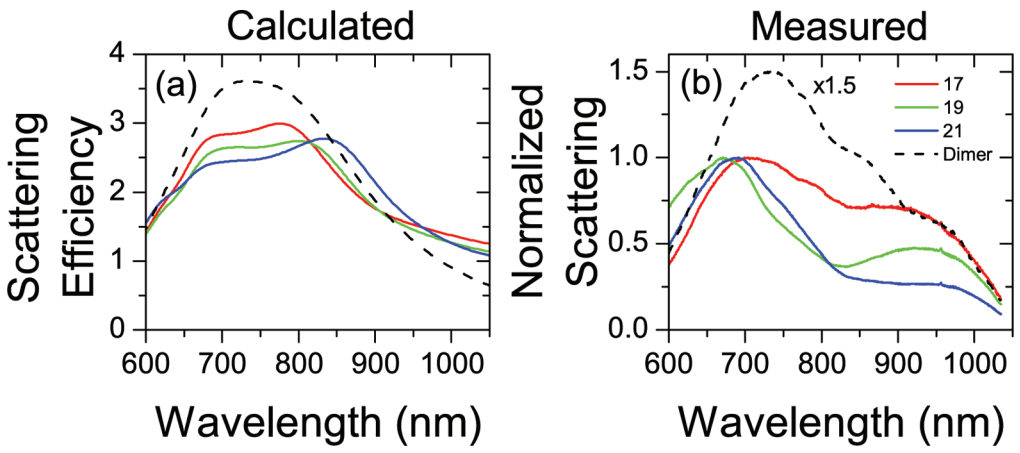

Figure 3. (a) Calculated scattering efficiency spectrum of an isolated dimer (black dashed line) as well as a dimer embedded in a heptadecagon (17), enneadecagon (19), and icosihenagon (21). (b) Normalized measured dark-field scattering spectra of the same geometries. Isolated dimer has been multiplied by 1.5 to facilitate comparison.

and is similarly located at 687 nm. The second scattering peak appears at 856 nm and is due to the photonic (*i.e.*, radiative) coupling between the dimer and heptadecagon. Because this low-energy peak is influenced by the geometry of the surrounding necklace, we expect that it will red shift when introducing more particles into the necklace. Below we will show that is indeed the case. Finally, a weak and broad scattering contribution is present in the CNNL scattering spectrum at approximately 1100 nm, which corresponds to the lowest energy heptadecagon peak.

We also investigate the scattering properties of a double-necklace CNNL, shown in Figure 2b. In this case, the geometry is a dimer/heptadecagon/tetracontagon. As with the single-necklace geometry, the two largest energy scattering peaks are centered at 673 and 804 nm, and a third low-energy peak at 983 nm arises due to the presence of the tetracontagon necklace. This leads to a scattering response that is broad-band over the 600−1000 nm wavelength range.

To confirm our calculations, we performed dark-field scattering measurements to determine the far-field properties of the isolated dimer and single-necklace CNNL geometries. We show in Figure 3a calculated scattering efficiencies of the dimer, dimer/heptadecagon, dimer/enneadecagon (19-particles), and dimer/icosihenagon (21-particles) geometries using unpolarized excitation. We expect the high-energy necklace peak to be mostly constant in wavelength with the number of particles in the necklace, and we expect a red shift in the low-energy necklace peak when more particles are added to the necklace.[14] Indeed, the high-energy peak remains stable while the low-energy peak red shifts, consistent with an increase in the necklace diameter. Figure 3b shows the measured dark-field scattering spectra for the same geometries. The isolated dimer spectrum has been multiplied by 1.5 to facilitate comparison. We notice a qualitatively good agreement in the CNNLs, which have two prevalent peaks and a noticeable red shift in the low-energy peak. Slight disagreements between theory and experiment are most likely due to minor deviations in particle shape and excitation conditions (high-angle dark-field experimental *vs* normal incidence plane wave calculations).[34]

Near-Field Optimization. We now turn our attention to the optimization of the near-field intensity in the dimer gap region in CNNLs, which is of fundamental importance in the design of plasmon-enhanced sensors. In Figure 4a, we show the calculated maximum near-field intensity spectra of a single-necklace CNNL, consisting of a dimer embedded into a pentadecagon (15-particle) through an icositridecagon (23-particle) necklace in increments of two particles. We observe a red shift of the wavelength of maximum near-field intensity as the surrounding necklace diameter increases. The maximum intensity near-field occurs spatially within the dimer gap. A smaller intensity peak occurring in the 1100−1200 nm region corresponds to the resonance of the necklace, with near-field hot-spots spatially residing in the necklace gap regions. We also see that there is a variation in the maximum value of the near-field intensity of each CNNL that is maximized by the dimer/enneadecagon geometry. We investigate this phenomenon in Figure 4b by plotting the maximum near-field intensity, which corresponds to the peak value of each spectrum from panel a (left axis, red), as a function of the number of particles in the surrounding necklace. Once again, we see the optimization for the dimer/enneadecagon CNNL. Concurrently, we show the wavelength where the maximum near-field occurs (right axis, blue). We see that the near-field resonance wavelength of the dimer, indicated by a dashed line, overlaps with the wavelength of the optimized CNNL. This suggests that the dimer/enneadecagon CNNL supports the strongest near-field due to the most efficient diffractive coupling between the dimer and the surrounding necklace.

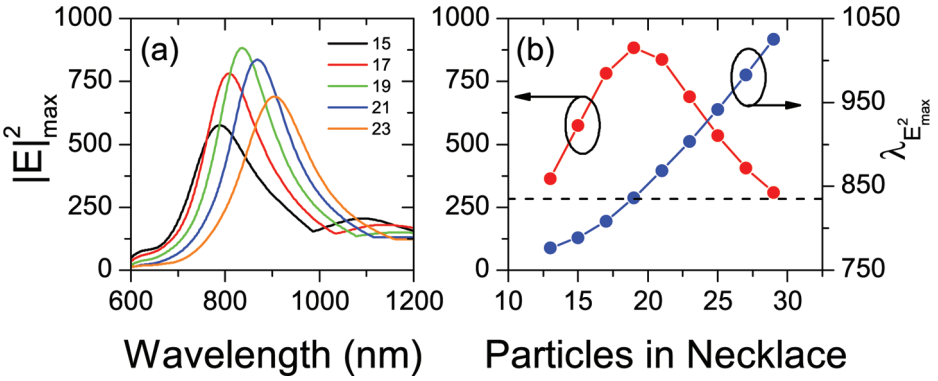

Figure 4. (a) Calculated maximum near-field intensity spectra of dimers embedded in 15−23-gons. (b) Maximum near-field intensity of each geometry (red curve, left axis) and wavelength corresponding to the maximum (blue curve, right axis) as a function of the number of particles in the necklace in which the dimer is embedded. Dashed line corresponds to the isolated dimer resonance at 833 nm.

Generalizing this analysis to multiple necklace CNNLs, we show that it is possible to further enhance the near-field intensity using higher-order radiative coupling from surrounding necklaces. By surrounding the optimized single-necklace CNNL into an even larger necklace, we calculate the near-field intensity within the dimer gap region. We found that the optimization occurs when the outer necklace has a diameter twice that of the inner necklace, with the collective CNNL resonance as close as possible to the individual dimer resonance. Building on the optimized dimer/enneadecagon geometry, we found that the optimal double-necklace CNNL consisted of a dimer/enneadecagon/tetracontagon. The tetracontagon necklace diameter is indeed twice that of the enneadecagon, which demonstrates second-order diffractive coupling. More generally, we found that the optimal necklace diameter for higher-order radiative coupling follows the formula $D = fN\lambda$, where N is the radiative order, λ is the resonance wavelength, and f is a constant scaling factor.

In Figure 5d, we show the near-field intensity spectra within the dimer gap region of a dimer (red), single-necklace CNNL (green), double-necklace CNNL (blue), triple-necklace CNNL (cyan), and so on to the seven-necklace CNNL (navy). The triple-necklace CNNL geometry consists of the optimized double-necklace CNNL embedded into an hexacontagon (60-particle) necklace, with all further CNNLs consisting of the previous optimized geometry surrounded by a necklace with an additional 20-particles (*i.e.*, the quadruple-necklace CNNL consists of the optimized triple-necklace CNNL surrounded by an octacontagon (80-particle) necklace). The inset shows the maximum near-field intensity for each geometry at the wavelength of maximum near-field in order to show the evolution of near-field optimization with the number of concentric necklaces in the CNNL. We show a clear increase in near-field intensity moving from the isolated dimer to single- and double-necklace CNNL

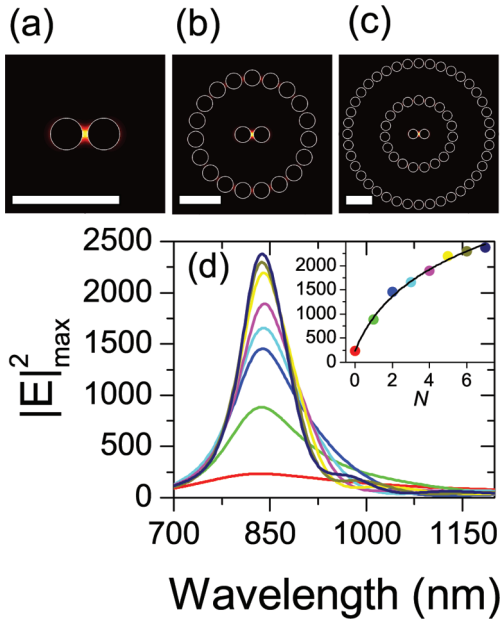

Figure 5. Calculated near-field intensity distributions at 785 nm of (a) isolated dimer, (b) dimer/enneadecagon, and (c) dimer/enneadecagon/tetracontagon. Scale bars correspond to 500 nm. (d) Near-field intensity spectra of an isolated dimer (red) embedded into optimized single (green), double (blue), triple (blue), through seven (navy) necklace(s). Inset shows the evolution of the maximum near-field intensity with the number of surrounding necklaces, *N*, fitted to a logarithmic function.

geometries, with a saturation effect once a third necklace is introduced into the arrangement. These data are fitted to a logarithmic function to show the scaling in near-fields as the number of necklaces (N) in the CNNL increases. These spectra show that the maximum near-field (resonance) wavelength for each geometry remains constant within a few nanometers of the individual dimer resonance, emphasizing the importance of efficient radiative coupling into the dimer. Furthermore, these near-field spectra are relatively broadband, which is important for sensing applications where near-fields must be optimized at more than one wavelength. In contrast to two-dimensional

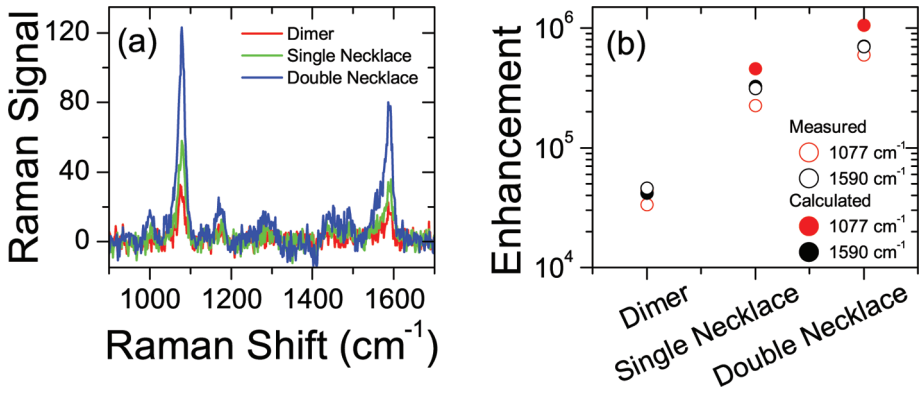

Figure 6. (a) Measured Raman spectra of a dimer, dimer/enneadecagon, and dimer/enneadecagon/tetracontagon. (b) Corresponding measured and calculated Raman enhancement factors of the 1077 and 1590 cm^{-1} pMA modes.

photonic–plasmonic gratings which exhibit spectrally narrow line shapes,[35,36] the CNNL arrangement is very suitable for sensing over a larger wavelength range, with a fwhm of 156, 134, and 118 nm for the single-, double-, and triple-necklace CNNLs.

Near-field spatial distributions provide important information regarding the location(s) of the hot-spot(s) in each CNNL geometry. In Figure 5a–c, we show the calculated spatial distributions of near-field intensity for isolated dimer, dimer/enneadecagon, and dimer/enneadecagon/tetracontagon geometries. Each scale bar corresponds to 500 nm. These near-field distributions are plotted at the wavelength of maximum near-field (approximately 833 nm in each case) and are normalized to their maxima. We demonstrate that the near-field at this optimized wavelength is concentrated primarily inside the subwavelength gap region of the dimer. This shows an efficient nanolensing effect into the dimer gap due to radiative coupling from the surrounding concentric necklaces.

In the following section, we will experimentally validate the predictions of near-field calculations using surface-enhanced Raman scattering measurements of pMA (*p*-mercaptoaniline) monolayers on fabricated CNNLs.

Surface-Enhanced Raman Scattering. Surface-enhanced Raman scattering is an inelastic light scattering process where incident light interacts with vibrational modes of a molecule residing on a nanostructured substrate that results in scattered light of a longer (Stokes-shifted) or shorter (anti-Stokes-shifted) wavelength.[37] SERS is a reliable technique for the identification of adsorbed molecules or for biological and chemical sensing.[38–40] SERS also acts as a tool to validate calculated near-fields at the wavelengths of the pump and Stokes-shifted modes.[6,41]

It has been shown that the enhancement factor of the Raman effect due to the substrate is $|E(\lambda_{exc})|^2|E(\lambda_s)|^2$, where λ_{exc} is the wavelength of the pump and λ_s the wavelength of the scattered signal.[42,43] Because of this, it is important to have strong near-fields at these two wavelengths in order to obtain very high Raman enhancements, as a strong Raman enhancement is necessary for sensing few or single molecules.[44] To this end, electromagnetic hot-spots are a good candidate for SERS devices as they concentrate strong near-fields into a small volume and have been studied in great detail.[25,45–47] Additionally, the regime of photonic–plasmonic coupling has also been studied in the context of SERS sensing.[48,49] As described above, CNNLs are uniquely suited to take advantage of the strong hot-spots created by quasi-static coupling of individual particles within the dimer as well as the radiative (photonic) coupling from surrounding necklaces. Indeed, the maximum intensity in CNNLs is stronger than that of individual dimers while remaining significantly enhanced over a broad spectral range.

In what follows, we perform surface-enhanced Raman scattering measurements on pMA monolayers adsorbed on the Au particles in dimers and CNNLs. pMA has been used as an analyte due to its widespread use in plasmonic SERS applications.[48,50]

Figure 6a shows the raw Stokes-shifted Raman signals experimentally measured from pMA monolayers on optimized isolated dimers, single-necklace CNNLs, and double-necklace CNNLs. We observe two predominant modes at 1077 and 1590 cm^{-1}. The measured signal is weakest for the dimers and strongest for the double-necklace CNNL in the absence of normalization. By focusing our calculations on the two pMA modes, we determine the Raman enhancement[44,50] for these geometries and compare to calculations from FDTD in Figure 6b.

It is important to note that local field intensity is primarily concentrated in the dimer gap region for all of the investigated structures (see Figure 5). For this reason, in our geometries, the central dimer area is the main contributor to the Raman effect since the enhancement scales with the intensity squared. Therefore, the surface area of the dimer should be used for the enhancement factor estimation for the different arrays.[41] This can be understood by defining a parameter %SERS, which is the ratio of the Raman

TABLE 1. %SERS Values for Isolated Dimer and Optimized CNNL Geometries

%SERS	1077 cm^{-1}	1590 cm^{-1}	dimer area ratio
isolated dimer	100%	100%	100%
single-necklace	76.4%	55.5%	9.5%
double-necklace	77.0%	70.8%	3.3%

enhancement contributed by the dimer to that contributed by all of the particles in the structure as

$$\%\mathrm{SERS} = \frac{\sum_{\mathrm{dimerarea}} |E_{\mathrm{pump}}|^2 |E_{\mathrm{Stokes}}|^2}{\sum_{\mathrm{totalarea}} |E_{\mathrm{pump}}|^2 |E_{\mathrm{Stokes}}|^2} \quad (1)$$

We obtained values for %SERS at both pMA modes using the calculated near-field intensity distributions of the isolated dimer, optimized single-necklace, and optimized double-necklace CNNLs and show the corresponding values in Table 1. The last column of this table shows the ratio of the dimer area as compared to the total Au area. From these data, we conclude that the illuminated dimer area contributes up to 75% of the Raman enhancement, while comprising less than 10% of the total Au surface area. Therefore, this normalization method enables a direct comparison among CNNLs and prevents significant underestimation of the Raman enhancement in the CNNL geometries.

Because the near-fields are concentrated predominantly in the dimer gap region, the enhancement is normalized to the Au surface area of the dimer for all geometries. FDTD calculations of the Raman enhancement are obtained by multiplying the maximum near-field intensity at the pump wavelength (785 nm) to the maximum near-field intensity at the Stokes-shifted wavelength (858 nm for the 1077 cm^{-1} mode and 897 nm for the 1590 cm^{-1} mode). The single-necklace CNNL shows a Raman enhancement 7× stronger than the isolated dimer for both the 1077 and 1590 cm^{-1} modes. An additional boost in enhancement is given by the double-necklace CNNL, which shows an enhancement over the dimer of 18 and 16× for the 1077 and 1590 cm^{-1} modes, respectively. The Raman enhancement values are all in excellent agreement with our predictions from FDTD.

The Raman enhancement factor was additionally determined for three single-necklace CNNL and three double-necklace CNNL geometries and are tabulated in Table 2. Calculations from FDTD are provided for comparison. Each of these measurements shows consistent agreement with calculated data, and the robustness of the Raman enhancement with slight perturbations in the number of particles in the smallest concentric necklace is shown. This robust behavior of the SERS signal is due to the broad-band nature of the near-fields, as demonstrated above in Figure 5.

TABLE 2. Measured and Calculated Raman Enhancement Factors

	1077 cm^{-1}		1059 cm^{-1}	
geometry	measured	calculated	measured	calculated
dimer	3.34×10^4	4.39×10^4	4.39×10^4	4.19×10^4
dimer in a necklace				
heptadecagon	2.62×10^5	3.24×10^5	3.24×10^5	3.04×10^5
enneadecagon	2.25×10^5	4.56×10^5	3.14×10^5	3.27×10^5
icosihenagon	2.06×10^5	2.64×10^5	3.24×10^5	2.43×10^5
dimer in a necklace in a tetracontagon				
heptadecagon	5.94×10^5	6.77×10^5	6.77×10^5	6.73×10^5
enneadecagon	5.99×10^5	1.06×10^6	6.96×10^5	7.07×10^5
icosihenagon	5.80×10^5	6.83×10^5	6.58×10^5	5.35×10^5

CONCLUSIONS

In this work, we have designed, fabricated, and experimentally characterized concentric necklace nanolenses (CNNLs) composed of a nanoparticle dimer positioned at the center of one or more concentric nanoplasmonic necklaces. We have shown that the far-field scattering resonances of CNNLs are strongly influenced by the coupling of the modes of the necklace(s) to that of the dimer, with two predominant scattering modes present in single-necklace CNNLs and three in double-necklace CNNLs. By changing the number of particles in the necklace component of the CNNL geometry, the near-field intensity at the dimer hot-spot is maximized when the diameter of the necklace is an integer multiple of the resonance wavelength of the dimer, multiplied by a constant scaling factor. We show that the intensity of the near-field in the dimer hot-spot continues to increase when more concentric necklaces are added and begins to saturate in a triple-necklace configuration. By performing SERS measurements of pMA monolayers on dimers and CNNLs, we demonstrate 7× Raman enhancement in the single-necklace and 18× enhancement in the double-necklace over the reference dimer geometry, with a maximum Raman enhancement value of approximately 7×10^5. The optimization of photonic–plasmonic coupling into a dimer hot-spot by the radiative coupling of concentric necklaces shows promise for applications in nanophotonic devices, optical nanoantennas, and nanoscale optical sensors.

METHODS

Nanoplasmonic Necklace Fabrication. All of the NP geometries studied in this paper were fabricated using an electron-beam lithography (EBL) process. A 180 nm coating of PMMA 950 (poly(methyl methacrylate)) resist was spun onto a quartz substrate and subsequently soft baked at 180 °C in an oven

for 20 min. During the e-beam writing, a sacrificial 10 nm Au coating was sputtered over the resist to eliminate charging of the substrate. EBL was performed with a Zeiss SUPRA 40VP SEM equipped with a Raith beam blanker and NPGS nanopatterning software. Samples were developed in MIBK (methyl isobutyl ketone) diluted in isopropyl alcohol. Using electron-beam evaporation, 28 nm of Au was deposited over a 2 nm Ti adhesion layer, and nanoparticles were formed by liftoff of the resist in acetone.

Finite-Difference Time-Domain Method. Three-dimensional FDTD simulations were performed using a commercial software package.[51] All NPs were modeled using the Au dispersion data as tabulated by Johnson and Christy[52] with diameter (150 nm) and height (30 nm) as dictated by fabrication parameters. In order to accurately model near-fields in and around the Au structures and ensure convergence in the simulation results, the mesh size around all of the NPs was set to 2.5 nm in the *x* and *y* (in-plane) dimensions and 2 nm in *z* (out-of-plane). Excitation was provided by a plane wave at normal incidence to the glass (n = 1.45) substrate. All simulations made use of perfectly matched layer (PML) boundary conditions were used to ensure absorption of electromagnetic radiation at the simulation boundaries.[53]

Dark-Field Spectroscopy. All experimental dark-field spectra were collected with an upright Olympus microscope (BX51WI) excited with unpolarized, incoherent, white halogen light. The excitation was coupled to the sample substrate using index-matching fluid between a dark-field condenser (NA = 1.2 to 1.4) and sample substrate and collected with a 40× (NA 0.65) objective. A pinhole with 2 mm diameter was placed before the condenser to limit the incident k-vectors and improve the overall spectral resolution. The transmitted signals were collected using an Andor Shamrock SR3030i grating spectrometer (150 lines/mm blazed at 500 nm) and CCD Andor DU401-BR-DD) electrically cooled to −75 °C. In order to ensure that the signals obtained were from only one array of CNNLs, the signal on the CCD was spatially filtered. All of the scattering spectra were background-corrected by subtraction of the scattering signal from an equal size, unpatterned area adjacent to each array and subsequently normalized by dividing the background-corrected spectra to the emission line shape of the excitation lamp.

SERS Detection. Nanoparticle samples were fabricated as above, plasma ashed in an oxygen environment for 10 min to eliminate contamination, and incubated in a 10 mM pMA solution in ethanol to form a self-assembled monolayer. After 12 h incubation, the samples were rinsed in neat ethanol. Each array of NPs was excited by a 785 nm diode laser with 20.5 mW output power fiber coupled to a 40× objective through the Olympus microscope described above, with the backscattered signal sent to the cooled CCD *via* the spectrometer using a grating with 600 lines/mm blazed at 750 nm. All Raman spectra were averaged over 10 measurements with a 0.1 s integration time. Prior to obtaining measurements from the NP arrays, the grating was first calibrated to the 520 cm^{-1} line of silicon.

Conflict of Interest: The authors declare no competing financial interest.

Acknowledgment. This work was partially supported by the NSF Career Award No. ECCS-0846651 and the AFOSR Award No. FA9550-10-1-0019.

REFERENCES AND NOTES

1. Hao, F.; Nehl, C. L.; Hafner, J. H.; Nordlander, P. Plasmon Resonances of a Gold Nanostar. *Nano Lett.* **2007**, *7*, 729–732.
2. Genet, C.; Ebbesen, T. W. Light in Tiny Holes. *Nature* **2007**, *445*, 39–46.
3. Forestiere, C.; Donelli, M.; Walsh, G. F.; Zeni, E.; Miano, G.; Dal Negro, L. Particle-Swarm Optimization of Broadband Nanoplasmonic Arrays. *Opt. Lett.* **2010**, *35*, 133–135.
4. Gopinath, A.; Boriskina, S. V.; Feng, N.-N.; Reinhard, B. M.; Negro, L. D. Photonic−Plasmonic Scattering Resonances in Deterministic Aperiodic Structures. *Nano Lett.* **2008**, *8*, 2423–2431.
5. Trevino, J.; Cao, H.; Dal Negro, L. Circularly Symmetric Light Scattering from Nanoplasmonic Spirals. *Nano Lett.* **2011**, *11*, 2008–2016.
6. Ye, J.; Wen, F.; Sobhani, H.; Lassiter, J. B.; Dorpe, P. V.; Nordlander, P.; Halas, N. J. Plasmonic Nanoclusters: Near Field Properties of the Fano Resonance Interrogated with SERS. *Nano Lett.* **2012**, *12*, 1660–1667.
7. Fan, J. A.; Wu, C.; Bao, K.; Bao, J.; Bardhan, R.; Halas, N. J.; Manoharan, V. N.; Nordlander, P.; Shvets, G.; Capasso, F. Self-Assembled Plasmonic Nanoparticle Clusters. *Science* **2010**, *328*, 1135–1138.
8. Hentschel, M.; Saliba, M.; Vogelgesang, R.; Giessen, H.; Alivisatos, A. P.; Liu, N. Transition from Isolated to Collective Modes in Plasmonic Oligomers. *Nano Lett.* **2010**, *10*, 2721–2726.
9. Hentschel, M.; Dregely, D.; Vogelgesang, R.; Giessen, H.; Liu, N. Plasmonic Oligomers: The Role of Individual Particles in Collective Behavior. *ACS Nano* **2011**, *5*, 2042–2050.
10. Lassiter, J. B.; Sobhani, H.; Fan, J. A.; Kundu, J.; Capasso, F.; Nordlander, P.; Halas, N. J. Fano Resonances in Plasmonic Nanoclusters: Geometrical and Chemical Tunability. *Nano Lett.* **2010**, *10*, 3184–3189.
11. Mirin, N. A.; Bao, K.; Nordlander, P. Fano Resonances in Plasmonic Nanoparticle Aggregates. *J. Phys. Chem. A* **2009**, *113*, 4028–4034.
12. Liu, N.; Mukherjee, S.; Bao, K.; Brown, L. V.; Dorfmüller, J.; Nordlander, P.; Halas, N. J. Magnetic Plasmon Formation and Propagation in Artificial Aromatic Molecules. *Nano Lett.* **2012**, *12*, 364–369.
13. Urzhumov, Y. A.; Shvets, G.; Fan, J. A.; Capasso, F.; Brandl, D.; Nordlander, P. Plasmonic Nanoclusters: A Path towards Negative-Index Metafluids. *Opt. Express* **2007**, *15*, 14129–14145.
14. Pasquale, A. J.; Reinhard, B. M.; Dal Negro, L. Engineering Photonic−Plasmonic Coupling in Metal Nanoparticle Necklaces. *ACS Nano* **2011**, *5*, 6578–6585.
15. Stockman, M. I. Nanofocusing of Optical Energy in Tapered Plasmonic Waveguides. *Phys. Rev. Lett.* **2004**, *93*, 137404.
16. Schuller, J. A.; Barnard, E. S.; Cai, W.; Jun, Y. C.; White, J. S.; Brongersma, M. L. Plasmonics for Extreme Light Concentration and Manipulation. *Nat. Mater.* **2010**, *9*, 193–204.
17. Ozbay, E. Plasmonics: Merging Photonics and Electronics at Nanoscale Dimensions. *Science* **2006**, *311*, 189–193.
18. Mühlschlegel, P.; Eisler, H.-J.; Martin, O. J. F.; Hecht, B.; Pohl, D. W. Resonant Optical Antennas. *Science* **2005**, *308*, 1607–1609.
19. Fang, Z.; Peng, Q.; Song, W.; Hao, F.; Wang, J.; Nordlander, P.; Zhu, X. Plasmonic Focusing in Symmetry Broken Nanocorrals. *Nano Lett.* **2011**, *11*, 893–897.
20. Bartal, G.; Lerosey, G.; Zhang, X. Subwavelength Dynamic Focusing in Plasmonic Nanostructures Using Time Reversal. *Phys. Rev. B* **2009**, *79*, 201103.
21. Maier, S. A. *Plasmonics: Fundamentals and Applications*, 1st ed.; Springer: Berlin, 2007.
22. Decker, M.; Feth, N.; Soukoulis, C. M.; Linden, S.; Wegener, M. Retarded Long-Range Interaction in Split-Ring-Resonator Square Arrays. *Phys. Rev. B* **2011**, *84*, 085416.
23. Khunsin, W.; Brian, B.; Dorfmüller, J.; Esslinger, M.; Vogelgesang, R.; Etrich, C.; Rockstuhl, C.; Dmitriev, A.; Kern, K. Long-Distance Indirect Excitation of Nanoplasmonic Resonances. *Nano Lett.* **2011**, *11*, 2765–2769.
24. Rycenga, M.; Camargo, P. H. C.; Li, W.; Moran, C. H.; Xia, Y. Understanding the SERS Effects of Single Silver Nanoparticles and Their Dimers, One at a Time. *J. Phys. Chem. Lett.* **2010**, *1*, 696–703.
25. Hao, E.; Schatz, G. C. Electromagnetic Fields around Silver Nanoparticles and Dimers. *J. Chem. Phys.* **2004**, *120*, 357–366.
26. Le Ru, E. C.; Grand, J.; Sow, I.; Somerville, W. R. C.; Etchegoin, P. G.; Treguer-Delapierre, M.; Charron, G.; Félidj, N.; Lévi, G.; Aubard, J. A Scheme for Detecting Every Single Target Molecule with Surface-Enhanced Raman Spectroscopy. *Nano Lett.* **2011**, *11*, 5013–5019.

27. Knight, M. W.; Sobhani, H.; Nordlander, P.; Halas, N. J. Photodetection with Active Optical Antennas. *Science* **2011**, *332*, 702–704.
28. Atwater, H. A.; Polman, A. Plasmonics for Improved Photovoltaic Devices. *Nat. Mater.* **2010**, *9*, 205–213.
29. Tang, L.; Kocabas, S. E.; Latif, S.; Okyay, A. K.; Ly-Gagnon, D.-S.; Saraswat, K. C.; Miller, D. A. B. Nanometre-Scale Germanium Photodetector Enhanced by a Near-Infrared Dipole Antenna. *Nat. Photonics* **2008**, *2*, 226–229.
30. Jiao, X.; Blair, S. Polarization Multiplexed Optical Bullseye Antennas. *Plasmonics* **2011**, 1–8.
31. Min, Q.; Santos, M. J. L.; Girotto, E. M.; Brolo, A. G.; Gordon, R. Localized Raman Enhancement from a Double-Hole Nanostructure in a Metal Film. *J. Phys. Chem. C* **2008**, *112*, 15098–15101.
32. Lerman, G. M.; Yanai, A.; Levy, U. Demonstration of Nanofocusing by the Use of Plasmonic Lens Illuminated with Radially Polarized Light. *Nano Lett.* **2009**, *9*, 2139–2143.
33. Chen, W.; Abeysinghe, D. C.; Nelson, R. L.; Zhan, Q. Plasmonic Lens Made of Multiple Concentric Metallic Rings under Radially Polarized Illumination. *Nano Lett.* **2009**, *9*, 4320–4325.
34. Knight, M. W.; Fan, J.; Capasso, F.; Halas, N. J. Influence of Excitation and Collection Geometry on the Dark Field Spectra of Individual Plasmonic Nanostructures. *Opt. Express* **2010**, *18*, 2579–2587.
35. Chu, Y.; Schonbrun, E.; Yang, T.; Crozier, K. B. Experimental Observation of Narrow Surface Plasmon Resonances in Gold Nanoparticle Arrays. *Appl. Phys. Lett.* **2008**, *93*, 181108.
36. Kravets, V. G.; Schedin, F.; Grigorenko, A. N. Extremely Narrow Plasmon Resonances Based on Diffraction Coupling of Localized Plasmons in Arrays of Metallic Nanoparticles. *Phys. Rev. Lett.* **2008**, *101*, 087403.
37. Le Ru, E.; Etchegoin, P. *Principles of Surface-Enhanced Raman Spectroscopy and Related Plasmonic E□ects*; Elsevier: Amsterdam, 2008.
38. Bolduc, O. R.; Masson, J.-F. Advances in Surface Plasmon Resonance Sensing with Nanoparticles and Thin Films: Nanomaterials, Surface Chemistry, and Hybrid Plasmonic Techniques. *Anal. Chem.* **2011**, *83*, 8057–8062.
39. Wang, Y.; Lee, K.; Irudayaraj, J. Silver Nanosphere SERS Probes for Sensitive Identification of Pathogens. *J. Phys. Chem. C* **2010**, *114*, 16122–16128.
40. Yan, B.; Thubagere, A.; Premasiri, W. R.; Ziegler, L. D.; Dal Negro, L.; Reinhard, B. M. Engineered SERS Substrates with Multiscale Signal Enhancement: Nanoparticle Cluster Arrays. *ACS Nano* **2009**, *3*, 1190–1202.
41. Forestiere, C.; Pasquale, A.; Capretti, A.; Miano, G.; Tamburrino, A.; Lee, S.; Reinhard, B. M.; Dal Negro, L. Genetically Engineered Plasmonic Nano-Arrays. *Nano Lett.* **2012**, *12*, 2037–2044.
42. Banaee, M. G.; Crozier, K. B. Mixed Dimer Double-Resonance Substrates for Surface-Enhanced Raman Spectroscopy. *ACS Nano* **2011**, *5*, 307–314.
43. Moskovits, M. Surface-Enhanced Spectroscopy. *Rev. Mod. Phys.* **1985**, *57*, 783–826.
44. Kneipp, K.; Kneipp, H.; Itzkan, I.; Dasari, R. R.; Feld, M. S. Surface-Enhanced Raman Scattering and Biophysics. *J. Phys.: Condens. Matter* **2002**, *14*, R597.
45. Ward, D. R.; Grady, N. K.; Levin, C. S.; Halas, N. J.; Wu, Y.; Nordlander, P.; Natelson, D. Electromigrated Nanoscale Gaps for Surface-Enhanced Raman Spectroscopy. *Nano Lett.* **2007**, *7*, 1396–1400.
46. Wang, H.; Levin, C. S.; Halas, N. J. Nanosphere Arrays with Controlled Sub-10-nm Gaps as Surface-Enhanced Raman Spectroscopy Substrates. *J. Am. Chem. Soc.* **2005**, *127*, 14992–14993.
47. Yan, B.; Boriskina, S. V.; Reinhard, B. M. Optimizing Gold Nanoparticle Cluster Configurations ($n = 7$) for Array Applications. *J. Phys. Chem. C* **2011**, *115*, 4578–4583.
48. Gopinath, A.; Boriskina, S. V.; Reinhard, B. M.; Dal Negro, L. Deterministic Aperiodic Arrays of Metal Nanoparticles for Surface-Enhanced Raman Scattering (SERS). *Opt. Express* **2009**, *17*, 3741–3753.
49. De Angelis, F.; Patrini, M.; Das, G.; Maksymov, I.; Galli, M.; Businaro, L.; Andreani, L. C.; Di Fabrizio, E. A Hybrid Plasmonic−Photonic Nanodevice for Label-Free Detection of a Few Molecules. *Nano Lett.* **2008**, *8*, 2321–2327.
50. Jackson, J. B.; Halas, N. J. Surface-Enhanced Raman Scattering on Tunable Plasmonic Nanoparticle Substrates. *Proc. Natl. Acad. Sci. U.S.A.* **2004**, *101*, 17930–17935.
51. Lumerical Solutions, Inc. http://www.lumerical.com/.
52. Johnson, P. B.; Christy, R. W. Optical Constants of the Noble Metals. *Phys. Rev. B* **1972**, *6*, 4370–4379.
53. Berenger, J.-P. A Perfectly Matched Layer for the Absorption of Electromagnetic Waves. *J. Comput. Phys.* **1994**, *114*, 185–200.